

Single-Chain Nanoparticles under Homogeneous Shear Flow

Maud Formanek[†] and Angel J. Moreno^{*,†,‡}

[†]*Centro de Física de Materiales (CSIC, UPV/EHU) and Materials Physics Center MPC,
Paseo Manuel de Lardizabal 5, E-20018 San Sebastián, Spain*

[‡]*Donostia International Physics Center (DIPC), Paseo Manuel de Lardizabal 4, E-20018
San Sebastián, Spain*

E-mail: angeljose.moreno@ehu.eus

Phone: +34 943 01 8845

Abstract

Single-chain nanoparticles (SCNPs) are a new class of macromolecular objects, synthesized through purely intramolecular cross-linking of single polymer chains. We use a multiscale hydrodynamics simulation approach to study, for the first time, SCNPs under shear flow. We investigate the case of irreversible SCNPs (permanent cross-links) in dilute solution. SCNPs emerge as a novel class of macromolecular objects with response to shear distinct from other systems such as linear chains, star polymers, rings or dendrimers. This is evidenced by the observed set of scaling exponents for the shear rate dependence of the SCNPs static and dynamic properties. Surprisingly these exponents are, at most, marginally dependent on the specific topology of the SCNPs (globular or sparse), suggesting that they are inherently related to the network-like character of the molecular architecture and not to its specific connectivity. At high Weissenberg numbers the dynamics of the sparse SCNPs is dominated by tumbling motion, whereas tank-treading predominates for the most globular SCNPs.

I. Introduction

Understanding the flow properties of macromolecular objects in solution is a problem of broad interest due to its relevance in many areas of soft matter, engineering and biophysics as e.g., microfluidics, extrusion or blood flow. There is nowadays strong evidence that the non-equilibrium conformations and reorientational dynamics under shear flow have a strong, and sometimes even dramatic, dependence on other features than the macromolecular concentration and shear rate. Thus, polymers under shear flow have been shown to exhibit a rich variety of dynamic behaviors depending on the type of bonding potentials,^{1,2} excluded volume interactions,³ hydrodynamics^{1,4,5} and, specially, on the molecular architecture.⁶⁻⁹ The two most commonly observed reorientational behaviors at high Weissenberg numbers (i.e., when the characteristic time of the flow is shorter than longest molecular relaxation time) are: (a) tumbling motion, which is characterized by the polymer alternately adapting stretched and collapsed conformations over the course of which it flips ‘head’ over ‘tail’ and (b) tank-treading motion, during which the overall shape of the polymer stays approximately constant and aligned with the flow, while the individual monomers perform a rotation around the center-of-mass. Flexible linear chains are the archetypical example of polymers performing tumbling motion, as extensively discussed theoretically,^{10,11} computationally¹²⁻¹⁶ and experimentally.¹⁷⁻²⁰ Tank treading has been found in weakly deformable soft objects as vesicles and fluid droplets.²¹⁻²⁴ For polymers of more complicated architectures, such as stars or rings, these two motions are not only hard to define (for example, what are the ‘ends’ of a ring to determine tumbling?), but also difficult to distinguish.^{1,2,25} Another remarkable effect of the molecular architecture is the observation of different sets of exponents for the shear rate dependence of the dynamic observables (viscosity, rotational frequency, etc) as well as the static observables probing alignment and deformations along the relevant directions (flow, gradient and vorticity).⁷

In this article we present detailed results that constitute, to the best of our knowledge, the first investigation on the static and dynamic properties under shear flow of the so-called single

chain nanoparticles (SCNPs).²⁶⁻³¹ These topologically complex soft nano-objects, which are obtained through purely intramolecular cross-linking of functionalized single linear chains, are the basis of the so-called single-chain technology, a rapidly growing research area of enormous potential for use as biosensors,³² catalysts,³³⁻³⁶ drug delivery vehicles,^{37,38} rheological agents,³⁹⁻⁴¹ etc. Inspired by biomacromolecules such as proteins or enzymes, it is a long-term goal³¹ to develop SCNPs via intramolecular collapse/folding with accurate control of the sequence and architecture, and with high-performance and quick response (due to their internal malleability) to environmental changes (pH, temperature, stress, etc). A series of works combining small angle neutron and X-ray scattering (SANS and SAXS) with computer simulations^{38,40,42,43} have revealed that the standard protocols of synthesis in good solvent conditions produce topologically polydisperse SCNPs, with a distribution dominated by sparse architectures. The fundamental physical origin of this observation is that, independently of the specific chemical composition of the precursor,^{44,45} the conformations of the SCNP in the good solvent conditions of synthesis are self-avoiding random walks (the polymer size scaling with the number of monomers as $R \sim N^\nu$, where $\nu \approx 0.59$ is the Flory exponent⁴⁶). In these configurations the formation of long-range loops is unfrequent, and most of the bonding events involve reactive groups separated by short contour distances, which are inefficient for the global compaction of the nanoparticle.⁴⁷⁻⁵² It is worth mentioning that the SCNP structure has interesting analogies with intrinsically disordered proteins (IDPs),^{53,54} starting with their scaling behavior ($R \sim N^\nu$, $\nu \sim 0.5$). Though, unlike IDPs, SCNPs lack regions with ordered secondary structure, they still contain weakly deformable ‘domains’ (dense clusters of permanent loops) connected by flexible segments. The peculiar architecture of SCNPs leads them to collapse to a so-called fractal globular structure⁵⁵⁻⁵⁷ in crowded solutions and melts, suggesting this as a potential scenario for the effect of the steric crowding on IDPs in cell environments.^{43,53}

Given their architectural complexity, their potential for a broad set of applications in solution and in bulk, and the mentioned structural analogies with IDPs, SCNPs are appealing

systems for the investigation of physical properties in flow. The first simulations of SCNPs under (homogeneous) shear flow presented here are limited to the case of high dilution. Properties in crowded solutions will be explored in future work. We have made use of the multi-particle collision dynamics^{58,59} technique, which correctly implements hydrodynamic interactions on long time scales. Several remarkable features are already found at high dilution. Thus, SCNPs emerge as a novel class of soft objects with a response to shear distinct from other flexible macromolecules such as linear chains, star polymers, rings or dendrimers. The differences with these architectures manifest in the set of characteristic exponents found for the shear rate dependence of the SCNP static and dynamic properties. Unexpectedly, these exponents show no significant dependence on the specific architecture of the SCNP, in spite of the broad distribution of investigated SCNP topologies (from globular to sparse ones). This suggests that the observed exponents are inherently related to the network-like character of the molecular architecture, but not to the specific connectivity of the network. At high Weissenberg numbers the dynamics of the sparsest SCNPs is dominated by tumbling motion, whereas tank-treading motion is predominant for the most globular ones.

The article is organized as follows. In Section II we give model and simulation details. Structural and dynamic observables under shear flow are characterized and discussed in Section III. Conclusions are given in Section IV.

II. Model and simulation details

We use a multi-scale hybrid simulation technique that combines molecular dynamics (MD) for the polymers with multi-particle collision dynamics (MPCD) for the solvent. The precursors of the SCNPs are modeled as linear chains of $N = 200$ monomers, of which a fraction $f = N_r/N = 0.25$ are functional reactive monomers. These have the ability to form irreversible crosslinks and are distributed randomly across the polymer backbone, with the constraint that they are never placed consecutively in order to avoid trivial crosslinks. We employ the

coarse-grained Kremer-Grest bead-spring model⁶⁰ to simulate both the precursor molecules and the synthesized SCNPs. As such, the non-bonded interactions between any two given monomers are modeled by a purely repulsive Lennard-Jones (LJ) potential,

$$U^{\text{LJ}}(r) = 4\epsilon \left[\left(\frac{\sigma}{r} \right)^{12} - \left(\frac{\sigma}{r} \right)^6 + \frac{1}{4} \right], \quad (1)$$

to account for excluded-volume interactions. Here, $r = |\mathbf{r}_i - \mathbf{r}_j|$ is the euclidean distance between monomers i and j , while $\epsilon/k_{\text{B}}T = 1$ and $\sigma = 1$ set the units of energy and length, respectively. We use a cutoff distance $r_c = 2^{1/6}\sigma$, at which both the potential and the corresponding forces are continuous. In addition, bonded monomers along the contour of the chain and cross-linked monomers interact via a finitely extensible nonlinear elastic (FENE) potential,⁶⁰

$$U^{\text{FENE}}(r) = -\epsilon K_{\text{F}} R_0^2 \ln \left[1 - \left(\frac{r}{R_0} \right)^2 \right], \quad (2)$$

with $K_{\text{F}} = 15\sigma^{-2}$ and $R_0 = 1.5\sigma$. This combination of LJ and FENE potentials limits the fluctuation of bonds and guarantees chain uncrossability, as well as mimicking good solvent conditions.

Our simulation protocol consists of two steps. First, 50 SCNPs are synthesized under highly dilute conditions without hydrodynamic interactions by employing Langevin dynamics simulations.⁶¹ The stochastic nature of the cross-linking process leads to all of the synthesized SCNPs having a distinct topology. A detailed description of the implementation of the cross-linking process can be found in Ref. 47. Briefly, permanent cross-links are formed between two reactive monomers that have not yet cross-linked to any other one and that are separated by less than the capture distance $r_{\text{b}} = 1.3\sigma$. In case there are multiple possible cross-linking partners for any given monomer at any given time, one of them is chosen at random. Finally, after the formation of a bond, the two involved monomers interact *via* the FENE potential introduced in 2 for the remainder of the simulation.

Next, we sort the 50 synthesized SCNPs into 6 groups based on the value of their as-

phericity parameter (see 6) and choose one from each group at random for the simulations under shear flow. In this way we study the effect of the SCNP shape by taking representatives of the whole distribution of asphericities. The solvent is modelled *via* MPCD,^{58,59} a mesoscopic particle-based technique for hydrodynamics simulations. The solvent is composed of N_s point-like particles of mass m , which correspond to individual volumes of the fluid. The MPCD algorithm consists of two alternating steps which govern the dynamics of the solvent: i) A *streaming* step, in which the solvent particles are propagated according to ballistic motion for a time h :

$$\mathbf{r}_i(t + \Delta t) = \mathbf{r}_i(t) + h\mathbf{v}_i(t), \quad (3)$$

with \mathbf{r}_i and \mathbf{v}_i the position and velocity of the solvent particle i . ii) A *collision* step, in which they exchange linear momentum. To achieve this, the particles are sorted into cubic cells of length a and subjected to a rotation around a random axis by an angle α with respect to the center-of-mass velocity of the cell \mathbf{v}_{cm} , i.e.

$$\mathbf{v}_i(t + \Delta t) = \mathbf{v}_{\text{cm}}(t) + \mathbf{R}(\alpha) (\mathbf{v}_i(t) - \mathbf{v}_{\text{cm}}(t)), \quad (4)$$

with $\mathbf{R}(\alpha)$ the rotation matrix. This conserves the total mass, linear momentum and energy of the system. To satisfy Galilean invariance, the cubic grid used to sort the particles has to be shifted randomly in each of the 3 directions at each collision step.^{62,63} A linear shear profile $\langle v_x(y) \rangle = \dot{\gamma}y$ is introduced *via* Lees-Edwards boundary conditions.⁶⁴ In the former expression $\dot{\gamma}$ is the shear rate, v_x the component of the velocity in the flow direction and y the coordinate in the simulation box along the gradient direction. 1 presents the setup of the simulation, showing the velocity profile and indicating the flow (x) and gradient (y) directions.

Since shear flow leads to viscous heating, a cell-level Maxwell-Boltzmann scaling thermostat is employed to keep the fluid at a fixed temperature T . Finally, the monomers of the

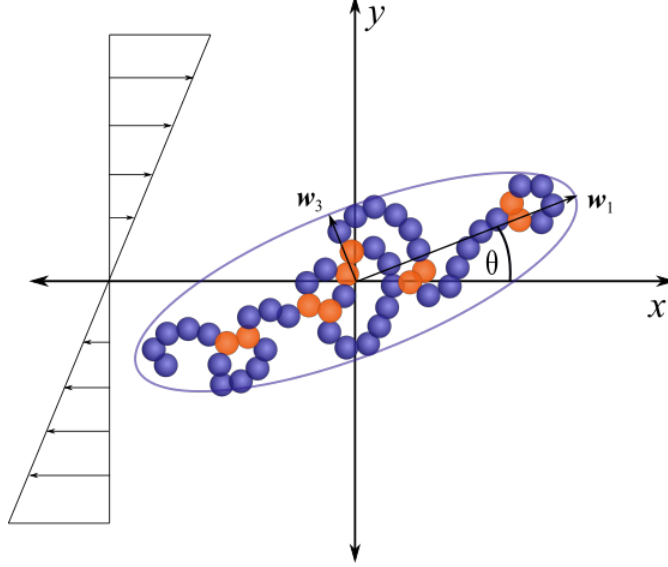


Figure 1: Schematic illustration of the simulation setup, indicating the fluid velocity profile as well as the eigenvalues and eigenvectors of the gyration tensor. Here, x is the flow direction, y the gradient direction and z – pointing perpendicular to the plane – is the vorticity direction. θ is the angle between the principal vector of the gyration tensor, \mathbf{w}_1 , and the flow direction. Reactive monomers forming cross-links are colored in orange, the rest in blue.

SCNPs are coupled to the solvent by including them in the collision step (4). It should be noted that this coupling is strong enough to ensure thermalization of the polymers as well as the solvent. Between successive collisions, the SCNP is propagated in time according to Newton’s equations of motion, which are integrated using the Velocity Verlet algorithm⁶⁵ with a time-step of $\Delta t = 0.01$. The number of solvent particles per cell is $\rho = 5$, their mass is $m = 1$, while the mass of the solute monomers is $M = \rho m = 5$. The remaining parameters are $\alpha = 130^\circ$, $h = 0.1\sqrt{ma^2/k_B T}$ and $a = \sigma = 1$. Furthermore, the volume of the simulation box $V = L_x L_y L_z$ is chosen based on the radius of gyration R_g of the SCNP at equilibrium ($\dot{\gamma} = 0$), such that $L_\mu = 50\sigma \geq 4R_g$ for $\mu \in \{y, z\}$. The extension of the box in the x -direction is increased with higher shear rates to account for the stretching of the SCNPs in the flow direction and ranges from $L_x = 50\sigma$ to $L_x = 100\sigma$. We perform 20 independent simulation runs for each shear rate $\dot{\gamma}$, with different initial conformations and velocities for each of the 6 individual SCNP topologies. Each run consists of an equilibration period over 10^5 MD steps and a production cycle of 10^7 MD steps.

For comparison with a linear reference system, we have performed analogous simulations and analysis for a linear chain with the same number of monomers, $N = 200$, as the SCNP. The corresponding observables discussed in the article for the SCNPs are shown in the Supporting Information for the linear chains (Figs S1-S4). These complement data for linear chains in the literature, which have been reported for much shorter chains ($N \leq 60$),⁶⁶ and for long DNA chains (combining experiments and numerical modelling).¹⁴ In spite of the differences in the used models (and in particular in the implementation of the interactions with the solvent), we find good agreement between the sets of exponents of the linear chains reported here and in those works (see 1).

III. Results and discussion

IIIA. Structural properties

The conformational properties of a polymer can be described by the gyration tensor

$$G_{\mu\nu} = \frac{1}{N} \sum_{i=1}^N (r_{i,\mu} - r_{\text{cm},\mu})(r_{i,\nu} - r_{\text{cm},\nu}), \quad (5)$$

where $r_{i,\mu}$ and $r_{\text{cm},\mu}$ are the μ -th Cartesian components of the position of monomer i and the center-of-mass, respectively. We calculate the eigenvalues $\lambda_1 \geq \lambda_2 \geq \lambda_3$ as well as the eigenvectors \mathbf{w}_i of the gyration tensor, which define an ellipsoid with the same inertial properties as the polymer. Various shape descriptors can be derived from the components as well as from the eigenvalues of the gyration tensor, such as the asphericity,

$$a = \frac{(\lambda_2 - \lambda_1)^2 + (\lambda_3 - \lambda_1)^2 + (\lambda_3 - \lambda_2)^2}{2(\lambda_1 + \lambda_2 + \lambda_3)^2}, \quad (6)$$

which ranges from 0 for objects with spherical symmetry to 1 for a one-dimensional object ($\lambda_2 = \lambda_3 = 0$). For each (topologically different) individual SCNP, its asphericity is averaged

over its 20 independent trajectories. The equilibrium asphericity $a_0 = a(\dot{\gamma} = 0)$ can be used to discern SCNPs in terms of their structure and it has been shown to correlate with the relative deformability $\delta = \sqrt{(\langle R_g^2 \rangle - \langle R_g \rangle^2) / \langle R_g^2 \rangle}$ of individual SCNPs.^{53,54} R_g is the molecular radius of gyration,

$$R_g^2 = \frac{1}{N} \sum_{i=1}^N (\mathbf{r}_i - \mathbf{r}_{\text{cm}})^2. \quad (7)$$

2 shows representative snapshots of 6 topologically different SCNPs in equilibrium ($\dot{\gamma} = 0$), covering the whole range of a_0 -values. The topological polydispersity in the SCNPs ranges from globular objects (left) to very open ones similar to self-avoiding chains (right), though the topological distribution is dominated by sparse architectures.

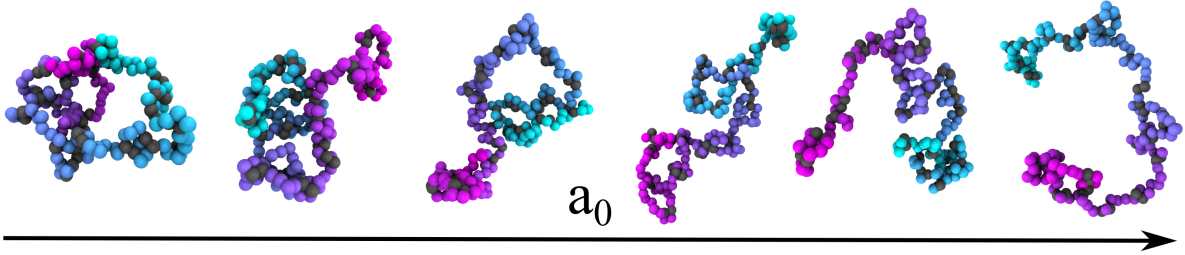


Figure 2: Representative snapshots of SCNPs at $\dot{\gamma} = 0$ with different values of the equilibrium asphericity a_0 (increasing from left to right). Grey beads are cross-linked monomers. The rest of the monomers are colored, from magenta to cyan, according to their position in the backbone of the linear precursor.

Since the specific topology of the individual SSCP may be expected to influence its response to shear and its relevant time scales, we introduce the dimensionless Weissenberg number, $Wi = \dot{\gamma}\tau_r$, to scale the shear rates. This parameter quantifies the ratio between the relaxation time τ_r of the polymer at equilibrium and the characteristic time $\dot{\gamma}^{-1}$ of the shear flow. To determine the relaxation time of the individual SCNPs, we introduce the autocorrelation function of the radius of gyration at zero shear rate,

$$C(t) = \frac{\langle R_g(t)R_g(0) \rangle - \langle R_g \rangle^2}{\langle R_g^2 \rangle - \langle R_g \rangle^2}, \quad (8)$$

and we define the relaxation time τ_r as the time at which $C(t)$ has decayed to 0.2. The

inset of 3 shows the autocorrelation function for representative SCNPs with very different topologies as measured by their deviation from spherical symmetry. We find that for most of the SCNP topologies $C(t)$ can be described by an exponential decay. 3a demonstrates that the equilibrium asphericity a_0 correlates with the relaxation time τ_r obtained from $C(t)$. The times encompass two decades and roughly scale as $\tau_r \sim a_0^2$.

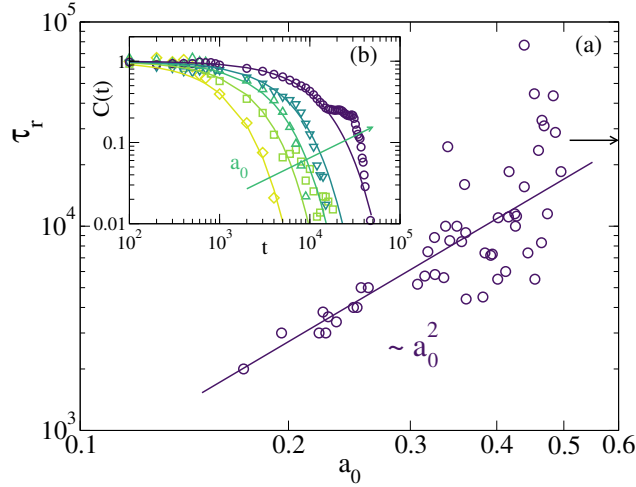


Figure 3: (a) Symbols: equilibrium ($\dot{\gamma} = 0$) relaxation times τ_r vs. equilibrium asphericity parameters a_0 of 50 topologically distinct SCNPs. The arrow indicates the τ_r of the linear chain. The inset (b) shows the autocorrelation function $C(t)$ of the radius of gyration R_g used to determine the relaxation times for 5 typical SCNPs. The arrow indicates increasing a_0 .

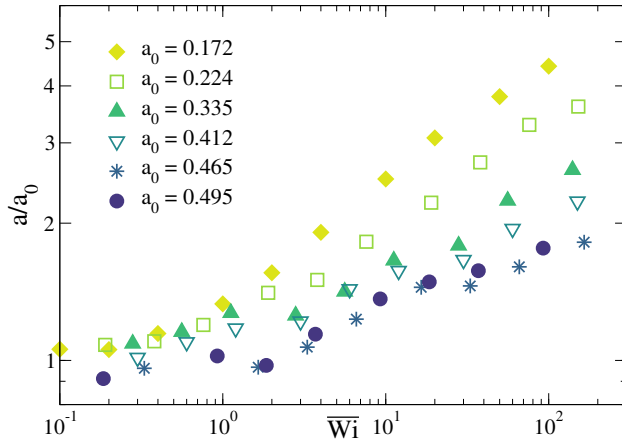


Figure 4: Normalized asphericity a as a function of the Weissenberg number Wi .

To investigate the effect of the shear flow on the structure of the SCNPs, in 4 we plot the normalized asphericity a/a_0 against the Weissenberg number Wi for 6 different SCNPs

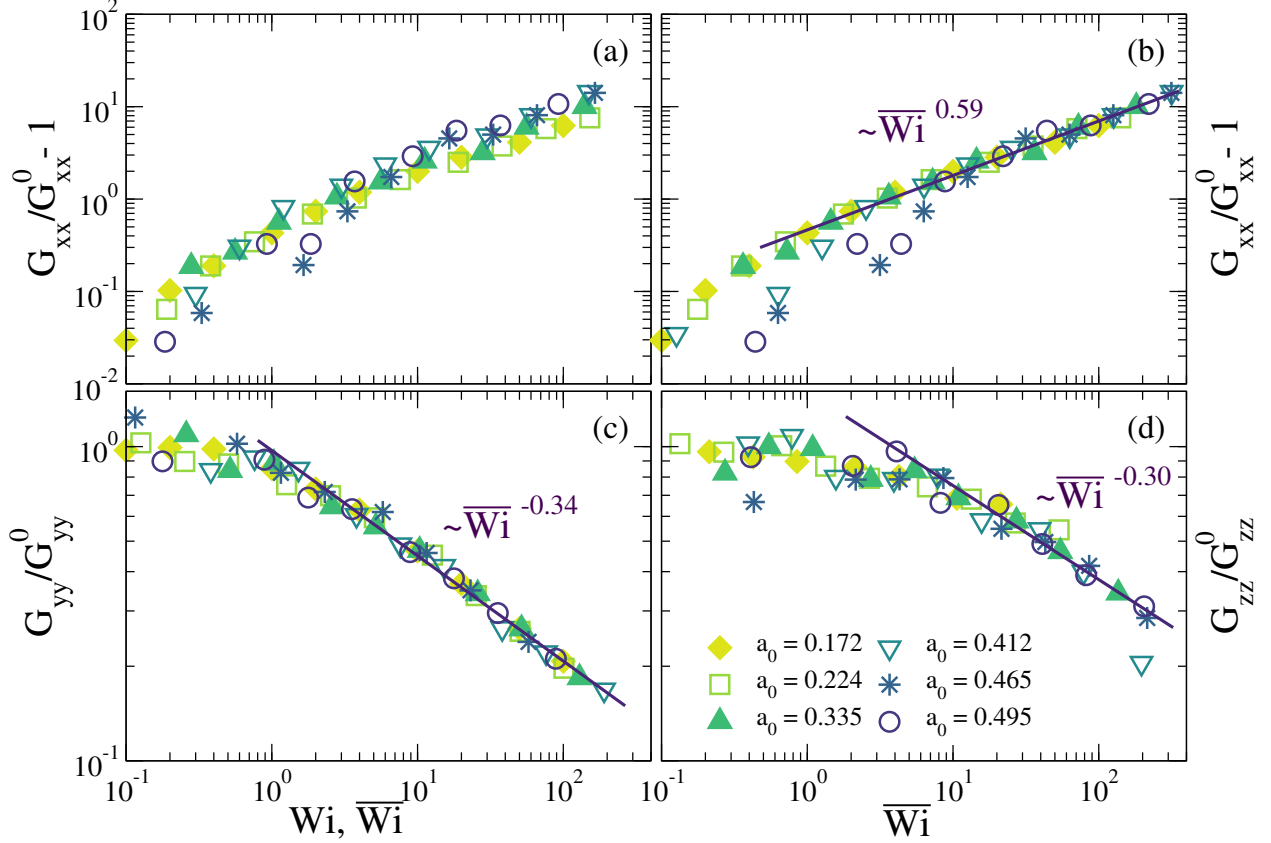


Figure 5: Normalized diagonal components of the gyration tensor $G_{\alpha\alpha}$ as a function of (a) Weissenberg number Wi and (b-d) rescaled Weissenberg number \overline{Wi} for various SCNP topologies of distinct equilibrium asphericities. Results are given for: (a,b) flow direction, G_{xx} ; (c) gradient direction, G_{yy} ; (d) vorticity direction, G_{zz} . Symbol codes have the same meaning across all panels. Lines are fits to power laws.

of equilibrium asphericities covering the whole range of a_0 values observed. Two regimes are clearly discernable: at small shear rates, where $Wi \ll 1$, the global shape of the SCNPs remains essentially undisturbed. When the longest relaxation time of the polymer τ_r exceeds the characteristic time of the flow $\dot{\gamma}^{-1}$, i.e. in the region where $Wi \gg 1$, the SCNP reorients in the flow field and adopts less spherical conformations. The fact that the cross-over between the two response regimes falls in the region where $Wi \approx 1$ for all SCNP topologies confirms the consistency of our method of determining the relaxation time τ_r . SCNPs of different topologies display different responses under high shear rates, with the shapes of SCNPs of low equilibrium asphericities a_0 being more affected than those of high a_0 values —still, it should be noted that actually the sparsest SCNPs ($a_0 \sim 0.5$) cannot be elongated beyond

the rod limit ($a = 1$) that is already approached at $Wi \sim 100$ (see 4).

Additional insights into the structural changes induced by the shear flow can be gained from considering the diagonal components of the gyration tensor, $G_{\alpha\alpha}$. 5 displays the components in the flow (G_{xx}), gradient (G_{yy}) and vorticity (G_{zz}) directions normalized by their values at zero shear rate ($G_{\alpha\alpha}^0$). Contrary to the changes in the asphericity with the shear rate, we find that the data for the different SCNPs collapse onto a master curve, when we rescale the Weissenberg number by a factor of the order of unity. This scaling factor should be inherently connected to the specific topology of the SCNP, in a similar fashion to, e.g., the case of star polymers, where the master curve is obtained after rescaling Wi by a factor dependent on the number of arms (functionality f).^{4,7} Panels (a) and (b) of 5 depict the diagonal component G_{xx} before and after rescaling the Weissenberg number and demonstrate that only a small scaling factor is required in order to obtain a master curve. For the remainder of the article, we will present the simulation results as a function of this rescaled Weissenberg number, \overline{Wi} . In the regime of high shear rates, all the diagonal components of the gyration tensor follow power laws, with exponents depending on the direction (flow, gradient, vorticity) but, within statistics, independent of the specific SCNP topology. The SCNPs stretch in the flow direction, $G_{xx} \sim Wi^\mu$ with $\mu = 0.59$, whereas they are compressed in both the gradient as well as the vorticity direction ($\mu = -0.34$ and -0.30 , respectively). As it will be shown, master curves $X \sim \overline{Wi}^\mu$ are obtained for the rest of the observables X computed for the SCNPs, with exponents depending on X but not on the specific topology of the SCNP (characterized by the equilibrium asphericity a_0). This result is unexpected given the very different topologies of SCNPs covering a rather broad range of asphericities (see 2), and therefore it seems related to the network-like topology of the SCNP but not the specific connectivity of the network.

As can be seen in 1, the stretching and compression behaviors probed by the components $G_{\alpha\alpha}$ of the gyration tensor are also observed as power laws, with different exponents, in other molecular architectures. The relative stretching of the SCNPs along the flow direction

is similar to that of linear chains and rings. This is consistent with the, in average, sparse character of the SCNP topology. The weaker dependence on the shear rate found for the SCNPs ($\mu = 0.59$ vs. 0.63 and 0.65 for linear chains and rings, respectively) likely originates from the cross-linked character of the SCNP that hinders elongation with respect to linear chains and rings. The apparently much stronger relative deformation of stars and dendrimers in the flow direction is analogous to the corresponding observation for the asphericity (4), i.e., molecular architectures that are already sparse in equilibrium have less margin of relative elongation than the spherical but still highly malleable stars and dendrimers.

The SCNPs show similar exponents for the relative compression along the gradient ($\mu = -0.34$) and vorticity ($\mu = -0.30$) directions. Regarding the compression along the gradient direction the SCNPs show a weaker Wi -dependence than linear chains and rings, and in this case SCNPs behave similar to dendrimers and high- f stars. A tentative explanation for this feature might be that the presence of cross-links (in the SCNPs) or branch points in the dense structures of dendrimers and high- f stars, combined with jamming, hinders compression in comparison with linear chains and rings. However, the SCNPs stretch in the flow direction more similarly to linear chains and rings because they frequently have long outer ends or loops that facilitate orientation of the principal axes with the flow. Regarding compression in the vorticity direction, the most malleable systems (linear chains, rings, low- f stars and SCNPs) show similar exponents $\mu \sim 0.3$, where a weak or marginal dependence on Wi is found for the high- f stars and dendrimers.

At this point it should be noted that, though a broad range of Wi -values of experimental interest is investigated here and in the references of 1, the exponents given for the $G_{\alpha\alpha}$ components, and for the other observables discussed in the rest of the article, may be just effective values in a slow crossover regime to the limit of high Weissenberg numbers ($Wi \gg 100$). For example, scaling arguments predict for linear chains an intermediate regime $G_{yy} \sim Wi^{-1/2}$ prior to the final regime $G_{yy} \sim Wi^{-2/3}$ reached in the high Wi -limit.^{6,70}

A measure of the average alignment of a macromolecule with the flow direction in the

Table 1: Scaling exponents for the Wi -dependence (at $Wi > 1$) of different static and dynamic observables, normalized by the values at $\dot{\gamma} = 0$, in SCNPs and other molecular architectures: linear chains, rings, 4th generation dendrimers (G4D) and star polymers. In the stars f is the number of arms (functionality) and N_a the number of monomers per arm. N is the total number of monomers in the macromolecule ($N = fN_a$ for the stars). Bold fonts: results from this work. Normal fonts: simulation results from the literature (references are indicated). Values in the third column were obtained by combining simulations and experiments in DNA chains.¹⁴ Values with star superscripts are not given in the original references; we have obtained them by sampling and fitting the data reported there.

	Linear $N = 200$	Linear (DNA) $N \leq 60$	Linear $N \leq 60$	Ring $N \leq 120$	G4D $N = 62$	Star $2N_a \leq 80$	SCNP $N = 200$
$G_{xx}/G_{xx}^0 - 1$	0.63			0.65^{25}	0.86^{67}	$1.0 (f \leq 50)^4$ $0.90^* (f = 18)^{68}$	0.59
G_{yy}/G_{yy}^0	-0.48	-0.50^{14}		$-0.41^{2,25}$	-0.30^{*67}	$-0.42 (f \leq 10)^7$ -0.32^* $(f = 18)^{68}$	-0.34
G_{zz}/G_{zz}^0	-0.34	-0.34^{14}		$-0.32^{2,25}$	$\approx 0^{*67}$	$-0.29 (f \leq 10)^7$ -0.14^* $(f = 18)^{68}$	-0.30
m_G	0.53	0.57^{14}	0.54^{66}	$0.60^{2,69}$	0.49^{67}	$0.63 (f \leq 10)^7$ $0.65 (f \leq 50)^{4,68}$	0.67
$\omega_z/\dot{\gamma}$	-1.0			$-0.38^{2,69}$		$-0.52 (f \leq 10)^7$ $-1.0 (f \leq 50)^4$	-0.75
η/η^0	-0.66	-0.61^{14}	-0.59^{66}	$-0.43^{2,25}$		$-0.40 (f \leq 10)^7$	-0.48
Φ_1/Φ_1^0	-1.2	-1.37^{14}	-1.2^{66}	-0.97^{25}		$-1.1 (f \leq 10)^7$	-1.2

presence of shear is given by the orientational resistance parameter⁷¹

$$m_G = Wi \tan(2\theta) = Wi \frac{2G_{xy}}{G_{xx} - G_{yy}}, \quad (9)$$

which can be directly calculated from the gyration tensor. It is related to the angle θ between the eigenvector \mathbf{w}_1 corresponding to the largest eigenvalue λ_1 and the flow direction x (see 1). For rodlike particles and linear polymers^{66,72,73} at low $\dot{\gamma}$ the components of the gyration tensor in 9 scale as $G_{xy} \sim \dot{\gamma}$ and $(G_{xx} - G_{yy}) \sim \dot{\gamma}^2$, such that at low shear rate m_G becomes independent of Wi . Computational investigations employing the same MPCD method as in

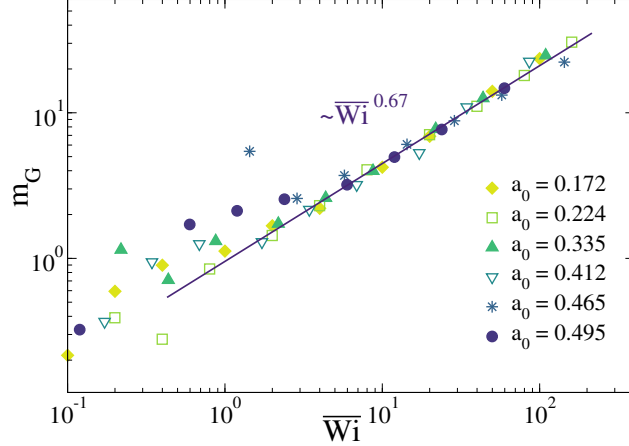


Figure 6: Orientational resistance m_G as a function of the rescaled Weissenberg number \overline{Wi} for SCNPs with different equilibrium asphericities.

this study have confirmed this behaviour also for star polymers.⁴

As can be seen in 6, however, the data for SCNPs do not clearly approach a plateau at low Wi , though no conclusions can be made due to the poor statistics at such low shear rates. Similar observations have been also found in, e.g., Ref. 67. The poor statistics originates from the denominator $G_{xx} - G_{yy}$ in 9, since at low shear rates the macromolecular conformations along the flow and gradient directions are weakly perturbed with respect to the equilibrium values $G_{xx}^0 = G_{yy}^0$. Moreover, the SCNPs simulated here are longer (larger N) than many of the previously studied systems (see 1), so that for the same value of the Weissenberg number the corresponding shear rate is even lower than in those systems. Still, we find that the data of m_G for different SCNP topologies again collapse onto a single curve upon applying the rescaling of the Weissenberg number. At high Wi , the orientational resistance follows a power law $m_G \sim Wi^\mu$ with exponent $\mu = 0.67$, which is comparable to that found for star polymers, $\mu = 0.65$,^{4,68} but considerably bigger than the one for linear chains, $\mu \sim 0.55$,^{14,66} or dendrimers, $\mu = 0.49$.⁶⁷ While in star polymers strong resistance to alignment with the flow originates from jamming in the two elongated bundles of arms (oriented in opposite directions in the stretched stars),⁴ in the SCNPs it might be explained by the existence of permanent loops and clusters of loops along the SCNP. This results again in strong repulsive forces, stemming from jamming within such loops and clusters, when the SCNP adopts

stretched conformations.

IIIB. Rheological properties

The contribution of the polymer to the viscosity of the dilute solution can be calculated from the Kramers-Kirkwood stress tensor,⁷⁴

$$\sigma_{\mu\nu} = \sum_{i=1}^N \langle r_{i,\mu} F_{i,\nu} \rangle, \quad (10)$$

where \mathbf{F}_i is the total force acting on monomer i and μ, ν denote the Cartesian components. The polymer contribution to the viscosity is then given by

$$\eta = \frac{\sigma_{xy}}{Wi}. \quad (11)$$

7a shows the viscosity η relative to the zero shear viscosity η_0 . Here η should be understood as the intrinsic viscosity,⁷⁵ since data correspond to the limit of dilute SCNPs. The definition of η includes a division by Wi . Therefore η_0 is usually determined by the Newtonian plateau of η at low shear rates $Wi \ll 1$. However, not all the SCNPs exhibit such a well-defined plateau, which is likely due to the big statistical uncertainty in $\sigma_{\mu\nu}$ at low Weissenberg numbers. Therefore, we normalize the viscosities such that the data collapse onto a single curve at high Weissenberg numbers. We find that the intrinsic viscosity of the SCNPs decreases with increasing Weissenberg number, alluding to shear-thinning behaviour, and that it scales as $\eta/\eta_0 \sim Wi^\mu$ with $\mu = -0.48$. This exponent is similar to those of stars and rings (see 1) and much smaller than the value found for linear chains ($\mu \sim -0.6$; $\mu = -2/3$ in the limit of high Weissenberg numbers^{6,70}). The stronger Wi -dependence of the viscosity in the linear chains can be rationalized by the lower compactness of their self-avoiding structure with respect to the other systems, and hence the higher concentration of solvent around each monomer.

In the absence of hydrodynamic interactions, the stress tensor can also be calculated

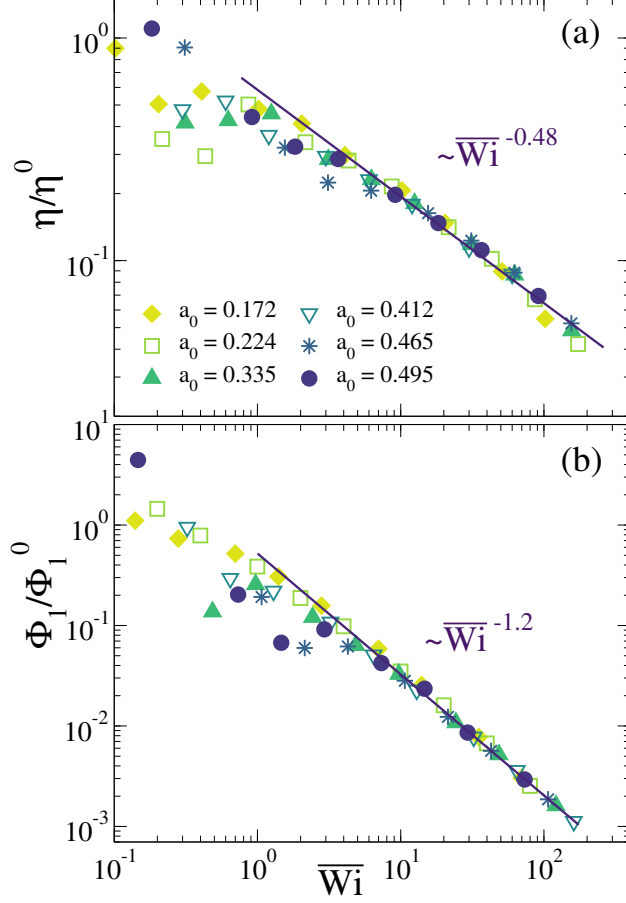


Figure 7: Normalized (a) viscosity η and (b) first normal stress coefficient Φ_1 as a function of the rescaled Weissenberg number \overline{Wi} for SCNPs with different equilibrium asphericities.

according to the Giesekus approximation,⁷⁵ which leads to

$$\eta = \sum_{i=1}^N \left\langle \frac{r_{i,y} r_{i,y}}{2} \right\rangle, \quad (12)$$

and thus $\eta \sim G_{yy}$. Agreement between η and G_{yy} has been found for linear chains in the free-draining limit,^{12,14} and for semidilute solutions of linear chains with hydrodynamic interactions⁷⁶ (where these are effectively screened out by the concentration). In the case of dilute macromolecules with hydrodynamic interactions the relation $\eta \sim G_{yy}$ clearly breaks for linear chains and SCNPs, as evidenced by the rather different exponents for the Wi -dependence of η and G_{yy} (see 1). This reflects the relevance of the hydrodynamic interactions in the rheological properties of linear chains and SCNPs, apparently playing a stronger role

than in low- f stars or rings, where η and G_{yy} show very similar scaling with the Weissenberg number (see 1).

In addition to the viscosity, we can also calculate the first normal stress coefficient from the stress tensor, i.e.,

$$\Phi_1 = \frac{\sigma_{xx} - \sigma_{yy}}{Wi^2}. \quad (13)$$

7b shows the first normal stress coefficient as a function of the rescaled Weissenberg number \overline{Wi} . Since $\sigma_{xx} - \sigma_{yy} \sim \dot{\gamma}^2$, a plateau is expected at low Weissenberg numbers. However, similar to the viscosity data, poor statistics at $Wi < 1$ complicates the identification of the zero-shear value in terms of a plateau, so we again scale Φ_1 such that the data collapse onto a master curve at high Wi . We find that the first normal stress coefficient decreases as $\Phi_1 \sim Wi^\mu$, with $\mu = -1.2$. This reflects a slightly weaker dependence than in linear polymers ($\mu \sim -1.3$; $\mu = -4/3$ according to scaling arguments),^{6,66,76} and slightly stronger than in low- f stars and rings ($\mu = -1.1$ and -0.97).²⁵

IIIC. Dynamic behavior

Tumbling motion is typically analyzed *via* the cross-correlation of the diagonal elements of the gyration tensor in the flow and gradient directions^{2,19,25,77}

$$C_{xy}(t) = \frac{\langle \delta G_{xx}(0) \delta G_{yy}(t) \rangle}{\sqrt{\langle \delta G_{xx}^2(0) \rangle \langle \delta G_{yy}^2(0) \rangle}}, \quad (14)$$

where $\delta G_{\alpha\beta} = G_{\alpha\beta} - \langle G_{\alpha\beta} \rangle$ is the fluctuation of a component of G around its mean value. Why this is a useful measure for detecting tumbling can be understood by looking at what happens during one tumbling event: for the majority of the time, the polymer is expanded in the flow direction to reduce stress from the current. However, thermal fluctuations lead to stochastic extensions of parts of the polymer in the gradient direction, whereupon those monomers experience an increased drag force from the flow and are pulled along the flow di-

rection. As a result, the polymer as a whole contracts to a coil, flips around and subsequently extends again in the flow direction, with the ‘head’ and the ‘tail’ having switched sides. Thus, tumbling is characterized by negative anti-correlation peaks in the cross-correlation function C_{xy} . Despite C_{xy} not being perfectly periodic but decaying to zero after some time, signatures of tumbling motion are clearly seen in 8.

Tank-treading, quite contrary to tumbling, is characterized by a lack of fluctuations of the polymer extension in either direction, while the individual monomers rotate around the polymer center-of-mass, leaving the overall shape unaffected. We follow the approach used by Chen *et al.*² to detect tank-treading behavior in ring polymers by calculating the angular auto-correlation function:

$$C_{\text{angle}}(t) = \frac{\langle A(0)A(t) \rangle}{\langle A^2(0) \rangle} \quad (15)$$

where $A(t) = \sin(2\beta)$ and β represents the angle between the vector connecting an individual monomer to the center-of-mass and the instantaneous first principal component of the polymer configuration. The averages in 15 are performed over the N monomers of the SCNP. If a polymer undergoes tank-treading, C_{angle} is expected to show an oscillating signal that is damped in time due to decorrelations arising from the intramolecular motions in the deformable polymer configuration.

We calculate both the flow-gradient extensional cross-correlation function $C_{xy}(t)$ as well as the angular auto-correlation function $C_{\text{angle}}(t)$ for different SCNP topologies. ?? show $C_{xy}(t)$ and $C_{\text{angle}}(t)$, respectively, for two SCNPs of intermediate (panels (a)) and low equilibrium asphericity (panels (b)). We find that both SCNPs show signs of a coexistence of tumbling and tank-treading behaviors at low and intermediate Wi . It should be noted that the periods of these motions differ with respect to the specific relaxation times τ_r of the polymers (see data in ?? where times are normalized by τ_r). Furthermore, the behavior of both SCNPs differs at high Weissenberg numbers. The SCNP of intermediate a_0 stops tank-treading and instead just performs tumbling cycles. The SCNP of low a_0 continues tank-treading up to the highest shear rate simulated (corresponding to $Wi = 100$ for this

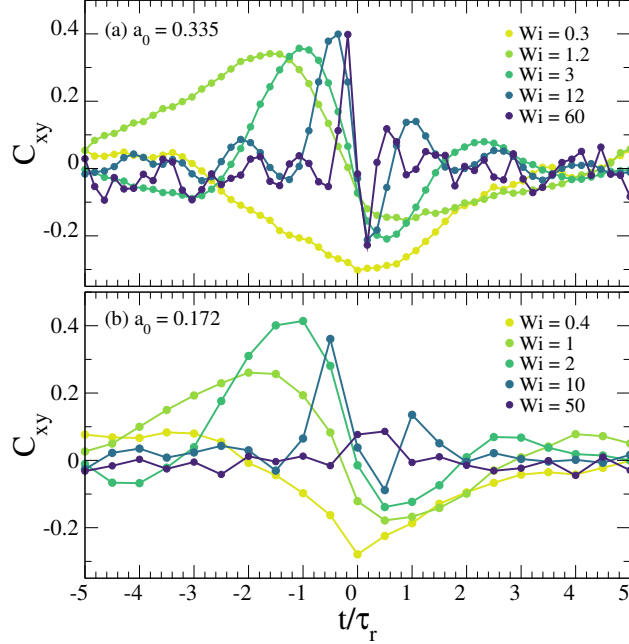


Figure 8: Flow-gradient extensional cross-correlation function $C_{xy}(t)$ for a SCNP of (a) intermediate and (b) low equilibrium asphericity. Times are rescaled by the longest relaxation time of the SCNP, τ_r .

SCNP), while the tumbling anti-correlation peak is lost already at $Wi = 50$ and instead shows a small positive peak centered around $t = 0$, suggesting some degree of simultaneity in the expansions (or contractions) in the gradient and flow direction. We note that SCNPs of higher equilibrium asphericity exhibit essentially the same behavior as the ones of intermediate asphericity, but the loss of tank-treading signatures in C_{angle} (not shown) occurs at a lower Wi .

To further investigate the difference in the dynamics between these two distinct SCNP topologies, we also plot (10) the distribution of the diagonal component of the gyration tensor in the flow direction, $P(G_{xx})$. We find that the intermediate asphericity SCNP (panel (a)) exhibits a significantly broader distribution and a less pronounced maximum across all Weissenberg numbers (note the logarithmic scale). The inset (10c) combines the data for $P(G_{xx})$ for both SCNPs in one graphic, but only for the two highest shear rates considered and in linear scales to highlight the maxima of the distributions. For the intermediate a_0 topology the maximum of the distribution does not shift much upon increasing the shear

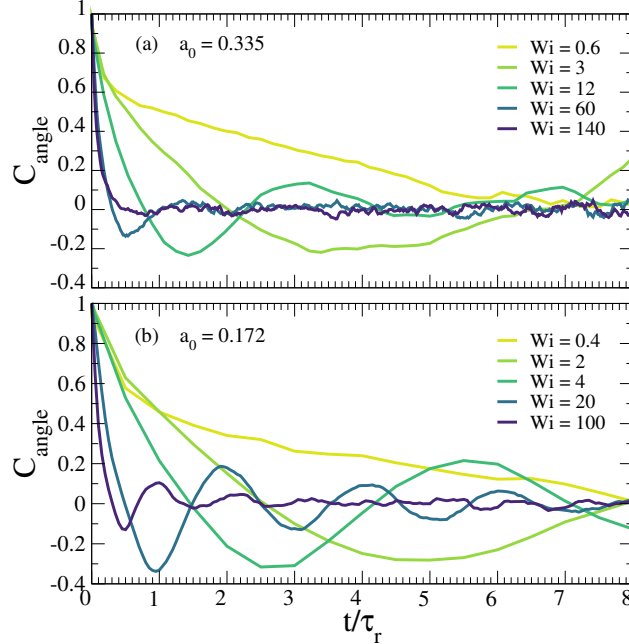


Figure 9: Angular auto-correlation function $C_{\text{angle}}(t)$ for a SCNP of (a) intermediate and (b) low equilibrium asphericity. Times are rescaled by the longest relaxation time of the SCNP, τ_r .

rate, but the tail of the distribution extends further to high G_{xx} values. The opposite is true for the low a_0 SCNP: by increasing Wi the width of the distribution $P(G_{xx})$ broadens only slightly, while the maximum shifts towards greater extension in the flow direction. These results are consistent with the interpretation that at high shear rates tumbling dominates the dynamics of the intermediate asphericity SCNP, whereas tank-treading is predominant in the low asphericity SCNP. Movies are included in the Supp. Info. (see description there) for the two former SCNPs, to illustrate the characteristic tumbling and tank-treading motions at high Wi . An example is also included for the low asphericity case at an intermediate Wi , for which tumbling (vanishing at higher Wi) still contributes significantly.

While the flow-gradient extensional cross-correlation function $C_{xy}(t)$ is used extensively in the literature to define tumbling behavior and has been linked to it through imaging studies of DNA,¹⁹ it does not in itself give any information about rotational dynamics. This has been pointed out by Sablić *et al.*¹ in a study of the dynamical behavior of star polymers, in which they relate the anti-correlation peaks in $C_{xy}(t)$ with ‘breathing’ modes of the star

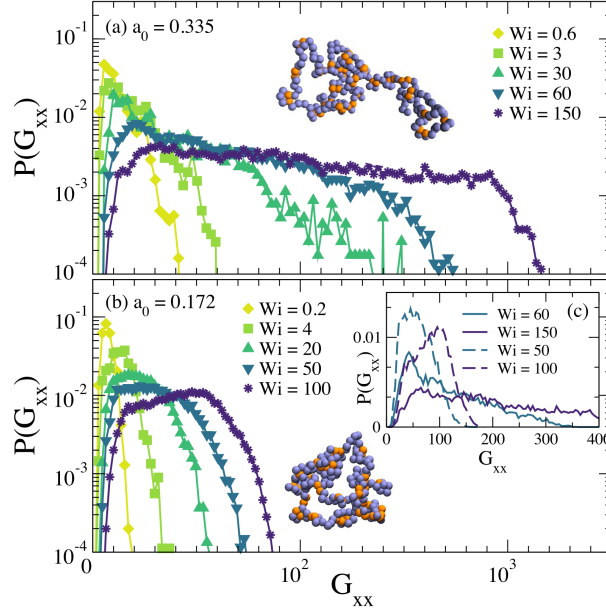


Figure 10: Probability distribution of the diagonal component of the gyration tensor in the flow direction, G_{xx} , as a function of the Weissenberg number Wi for a SCNP of (a) intermediate and (b) low equilibrium asphericity (log-lin scale). The inset (c) compares $P(G_{xx})$ of the two topologies at intermediate and high Weissenberg numbers on a lin-lin scale. Full lines in this inset represent the SCNP of intermediate asphericity ($a_0 = 0.335$), while dashed lines represent the SCNP of low asphericity ($a_0 = 0.172$). Snapshots of typical equilibrium conformations are included to highlight the different topologies.

rather than tumbling. In this regard, we calculate the rotational frequency of the SCNPs in the vorticity direction by making use of the geometrical approximation^{78,79}

$$\omega_z/\dot{\gamma} = \frac{\langle G_{yy} \rangle}{\langle G_{xx} \rangle + \langle G_{yy} \rangle}, \quad (16)$$

which is based on the rigid-body relation $\mathbf{L} = \mathbf{J}\boldsymbol{\omega}_{\mathbf{L}}$ and relates the angular momentum \mathbf{L} to the rotational frequency $\boldsymbol{\omega}_{\mathbf{L}}$ via the inertia tensor \mathbf{J} . In the derivation of the geometrical approximation of 16 it is assumed that the velocity of the monomers is governed purely by the undisturbed velocity profile of the fluid ($v_x \simeq \dot{\gamma}y$) and that rotation only manifests around the vorticity axis, i.e. $\omega_x = \omega_y \approx 0$. Sablić *et al.*¹ compiled data from studies of different polymer architectures, bonding potentials as well as hydrodynamic simulation techniques, and found good agreement between ω_L and ω_z over a broad range of Weissenberg numbers.

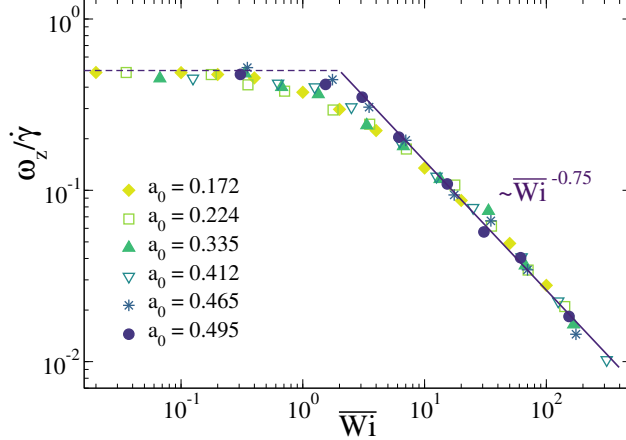


Figure 11: Rotational frequency ω_z as a function of the rescaled Weissenberg number \overline{Wi} for SCNPs with different equilibrium asphericities.

Since the rotational frequency of soft objects is expected to scale linearly with the shear rate for low Wi , we report our results as a reduced rotational frequency $\omega_z/\dot{\gamma}$ versus \overline{Wi} in 11. The data are found to approach the expected linear scaling $\omega_z \simeq \dot{\gamma}/2$ at small \overline{Wi} for all SCNP topologies. For large shear rates, the data collapse onto a master curve as well, when plotted against the rescaled Weissenberg number \overline{Wi} , and scale as $\omega_z/\dot{\gamma} \sim \overline{Wi}^{-0.75}$. This common scaling for the rotational frequency is somewhat unexpected, given the rather different dynamic behaviors displayed at large Wi by the $C_{xy}(t)$ and $C_{\text{angle}}(t)$ correlators (with predominance of tumbling or tank-treading motions depending on the SCNP topology). Still, one should keep in mind that both ω_L and ω_z are based on a generalization of rigid-body rotations to soft objects, and therefore correspond to the rotation of a rigid-body having the average shape of the polymer. Interpretation of ω_z as an angular velocity to quantify either the tumbling or the tank-treading frequency suffers from the fact that rotational vibrations are included in the calculation of ω_z , which do not add to the molecule overall rotation. Recent studies^{9,80} have suggested to use the co-rotating Eckart frame⁸¹ to decouple rotations from vibrations and thus better understand the dynamics of soft objects. An in-depth analysis of the rotational dynamics of the various SCNP topologies in terms of the Eckart formalism is beyond the scope of this work and will be studied in a future work. As can be seen in 1, the exponents found for the Wi -dependence of the rotational frequency

(as defined in 16) for the different topologies show a strong dispersion and no obvious trend. The use of the Eckart frame to determine the rotational frequency might shed light on this question.

IV. Conclusions

By means of a coarse-grained polymer model, combined with multi-particle collision dynamics to implement hydrodynamic interactions, we have investigated SCNPs under homogeneous shear flow. SCNPs emerge as a novel class of complex macromolecular objects with a response to shear that is distinct from other polymeric objects such as linear chains, rings, dendrimers or stars. This is demonstrated by the unique set of scaling exponents for the shear rate dependence of static and dynamic observables as the components of the gyration tensor, orientational resistance, intrinsic viscosity or rotational frequency. Surprisingly, the obtained sets of exponents are, at most, marginally dependent on the specific topology of the SCNP (globular or sparse). This suggests that the response of SCNPs to shear is inherently related to the network-like character of their molecular architecture, but not the specific connectivity of the network. By analyzing adapted time correlation functions we have found that at high Weissenberg numbers the dynamics of the sparse SCNPs is dominated by tumbling motion. Tank-treading is predominant for the most globular SCNPs.

The general physical scenario presented here may motivate not only experimental tests in SCNPs but also in intrinsically disordered proteins, given the observed structural similarities between both systems.^{53,54} Another question to be investigated is the effect of the concentration of SCNPs on their response to shear. Investigations in semidilute solutions (up to a few times the overlap concentration) of unentangled or weakly entangled linear chains^{82,83} and star polymers^{79,84,85} have shown small or moderate changes in the characteristic exponents for the Wi -dependence with respect to those found at high dilution. It is not obvious how the high-dilution scenario for the SCNP behavior under shear flow will be affected by increasing

concentration, since in equilibrium SCNPs are indeed more strongly perturbed by crowding (collapsing to fractal globular structures^{43,53}) than linear chains. Work in this direction is in progress.

Acknowledgement

We acknowledge financial support from the projects MAT2015-63704-P (MINECO-Spain and FEDER-UE) and IT-654-13 (Basque Government, Spain).

References

- (1) Sablić, J.; Praprotnik, M.; Delgado-Buscalioni, R. *Soft Matter* **2017**, *13*, 4971–4987.
- (2) Chen, W.; Chen, J.; Liu, L.; Xu, X.; An, L. *Macromolecules* **2013**, *46*, 7542–7549.
- (3) Chen, W.; Zhao, H.; Liu, L.; Chen, J.; Li, Y.; An, L. *Soft Matter* **2015**, *11*, 5265–5273.
- (4) Ripoll, M.; Winkler, R. G.; Gompper, G. *Phys. Rev. Lett.* **2006**, *96*, 188302.
- (5) Liebetreu, M.; Ripoll, M.; Likos, C. N. *ACS Macro Lett.* **2018**, *7*, 447–452.
- (6) Winkler, R. G.; Fedosov, D. A.; Gompper, G. *Curr. Opin. Colloid Interface Sci.* **2014**, *19*, 594 – 610.
- (7) Chen, W.; Zhang, K.; Liu, L.; Chen, J.; Li, Y.; An, L. *Macromolecules* **2017**, *50*, 1236–1244.
- (8) Jeong, S. H.; Kim, J. M.; Baig, C. *Macromolecules* **2017**, *50*, 4491–4500.
- (9) Jaramillo-Cano, D.; Likos, C. N.; Camargo, M. *Polymers* **2018**, *10*.
- (10) Puliafito, A.; Turitsyn, K. *Physica D* **2005**, *211*, 9 – 22.
- (11) Winkler, R. G. *Phys. Rev. Lett.* **2006**, *97*, 128301.

- (12) Doyle, P. S.; Shaqfeh, E. S. G.; Gast, A. P. *J. Fluid Mech.* **1997**, *334*, 251–291.
- (13) Hur, J. S.; Shaqfeh, E. S. G.; Larson, R. G. *J. Rheol.* **2000**, *44*, 713–742.
- (14) Schroeder, C. M.; Teixeira, R. E.; Shaqfeh, E. S. G.; Chu, S. *Macromolecules* **2005**, *38*, 1967–1978.
- (15) Dalal, S. I.; Albaugh, A.; Hoda, N.; Larson, R. G. *Macromolecules* **2012**, *45*, 9493–9499.
- (16) Lang, P. S.; Obermayer, B.; Frey, E. *Phys. Rev. E* **2014**, *89*, 022606.
- (17) Smith, D. E.; Babcock, H. P.; Chu, S. *Science* **1999**, *283*, 1724–1727.
- (18) Hur, J. S.; Shaqfeh, E. S. G.; Babcock, H. P.; Smith, D. E.; Chu, S. *J. Rheol.* **2001**, *45*, 421–450.
- (19) Teixeira, R. E.; Babcock, H. P.; Shaqfeh, E. S. G.; Chu, S. *Macromolecules* **2005**, *38*, 581–592.
- (20) Gerashchenko, S.; Steinberg, V. *Phys. Rev. Lett.* **2006**, *96*, 038304.
- (21) Skotheim, J. M.; Secomb, T. W. *Phys. Rev. Lett.* **2007**, *98*, 078301.
- (22) Abkarian, M.; Faivre, M.; Viallat, A. *Phys. Rev. Lett.* **2007**, *98*, 188302.
- (23) Dodson, W.; Dimitrakopoulos, P. *Biophys. J.* **2010**, *99*, 2906 – 2916.
- (24) Yazdani, A. Z. K.; Bagchi, P. *Phys. Rev. E* **2011**, *84*, 026314.
- (25) Chen, W.; Li, Y.; Zhao, H.; Liu, L.; Chen, J.; An, L. *Polymer* **2015**, *64*, 93 – 99, New application of Organic Reactions for Controlling Polymer Architectures (ORCP).
- (26) Altintas, O.; Barner-Kowollik, C. *Macromol. Rapid Commun.* **2016**, *37*, 29–46.
- (27) Lyon, C. K.; Prasher, A.; Hanlon, A. M.; Tuten, B. T.; Tooley, C. A.; Frank, P. G.; Berda, E. B. *Polym. Chem.* **2015**, *6*, 181–197.

- (28) Gonzalez-Burgos, M.; Latorre-Sanchez, A.; Pomposo, J. A. *Chem. Soc. Rev.* **2015**, *44*, 6122–6142.
- (29) Mavila, S.; Eivgi, O.; Berkovich, I.; Lemcoff, N. G. *Chem. Rev.* **2016**, *116*, 878–961.
- (30) Hanlon, A. M.; Lyon, C. K.; Berda, E. B. *Macromolecules* **2016**, *49*, 2–14.
- (31) Pomposo, J. A., Ed. *Single-Chain Polymer Nanoparticles: Synthesis, Characterization, Simulations, and Applications*; John Wiley & Sons: Weinheim, Germany, 2017.
- (32) Gillissen, M. A. J.; Voets, I. K.; Meijer, E. W.; Palmans, A. R. A. *Polym. Chem.* **2012**, *3*, 3166–3174.
- (33) Terashima, T.; Mes, T.; De Greef, T. F. A.; Gillissen, M. A. J.; Besenius, P.; Palmans, A. R. A.; Meijer, E. W. *J. Am. Chem. Soc.* **2011**, *133*, 4742–4745.
- (34) Perez-Baena, I.; Barroso-Bujans, F.; Gasser, U.; Arbe, A.; Moreno, A. J.; Colmenero, J.; Pomposo, J. A. *ACS Macro Lett.* **2013**, *2*, 775–779.
- (35) Huerta, E.; Stals, P. J. M.; Meijer, E. W.; Palmans, A. R. A. *Angew. Chem. Int. Ed.* **2013**, *52*, 2906–2910.
- (36) Tooley, C. A.; Pazicni, S.; Berda, E. B. *Polym. Chem.* **2015**, *6*, 7646–7651.
- (37) Hamilton, S. K.; Harth, E. *ACS Nano* **2009**, *3*, 402–410.
- (38) Sanchez-Sanchez, A.; Akbari, S.; Moreno, A. J.; Lo Verso, F.; Arbe, A.; Colmenero, J.; Pomposo, J. A. *Macromol. Rapid Commun.* **2013**, *34*, 1681–1686.
- (39) Mackay, M. E.; Dao, T. T.; Tuteja, A.; Ho, D. L.; Horn, B. V.; Kim, H.-C.; Hawker, C. J. *Nat. Mater.* **2003**, *2*, 762–766.
- (40) Arbe, A.; Pomposo, J.; Moreno, A.; LoVerso, F.; Gonzalez-Burgos, M.; Asenjo-Sanz, I.; Iturrospe, A.; Radulescu, A.; Ivanova, O.; Colmenero, J. *Polymer* **2016**, *105*, 532 – 544.

- (41) Bačová, P.; Lo Verso, F.; Arbe, A.; Colmenero, J.; Pomposo, J. A.; Moreno, A. J. *Macromolecules* **2017**, *50*, 1719–1731.
- (42) Basasoro, S.; Gonzalez-Burgos, M.; Moreno, A. J.; Verso, F. L.; Arbe, A.; Colmenero, J.; Pomposo, J. A. *Macromol. Rapid Commun.* **2016**, *37*, 1060–1065.
- (43) Gonzalez-Burgos, M.; Arbe, A.; Moreno, A. J.; Pomposo, J. A.; Radulescu, A.; Colmenero, J. *Macromolecules* **2018**, *51*, 1573–1585.
- (44) Pomposo, J. A.; Perez-Baena, I.; Lo Verso, F.; Moreno, A. J.; Arbe, A.; Colmenero, J. *ACS Macro Lett.* **2014**, *3*, 767–772.
- (45) Pomposo, J. A.; Rubio-Cervilla, J.; Moreno, A. J.; Lo Verso, F.; Bacova, P.; Arbe, A.; Colmenero, J. *Macromolecules* **2017**, *50*, 1732–1739.
- (46) Rubinstein, M.; Colby, R. H. *Polymer Physics*; Oxford University Press: Oxford, U.K., 2003; Vol. 23.
- (47) Moreno, A. J.; Lo Verso, F.; Sanchez-Sanchez, A.; Arbe, A.; Colmenero, J.; Pomposo, J. A. *Macromolecules* **2013**, *46*, 9748–9759.
- (48) Lo Verso, F.; Pomposo, J. A.; Colmenero, J.; Moreno, A. J. *Soft Matter* **2014**, *10*, 4813–4821.
- (49) Lo Verso, F.; Pomposo, J. A.; Colmenero, J.; Moreno, A. J. *Soft Matter* **2015**, *11*, 1369–1375.
- (50) Rabbal, H.; Breier, P.; Sommer, J.-U. *Macromolecules* **2017**, *50*, 7410–7418.
- (51) Formanek, M.; Moreno, A. J. *Soft Matter* **2017**, *13*, 6430–6438.
- (52) Oyarzun, B.; Mognetti, B. M. *J. Chem. Phys.* **2018**, *148*, 114110.
- (53) Moreno, A. J.; Lo Verso, F.; Arbe, A.; Pomposo, J. A.; Colmenero, J. *J. Phys. Chem. Lett.* **2016**, *7*, 838–844.

- (54) Moreno, A. J.; Bacova, P.; Verso, F. L.; Arbe, A.; Colmenero, J.; Pomposo, J. A. *J. Phys.: Condens. Matter* **2018**, *30*, 034001.
- (55) Grosberg, A. Y.; Nechaev, S. K.; Shakhnovich, E. I. *J. Phys. (Paris)* **1988**, *49*, 2095–2100.
- (56) Mirny, L. A. *Chromosome Res.* **2011**, *19*, 37–51.
- (57) Halverson, J. D.; Smrek, J.; Kremer, K.; Grosberg, A. Y. *Rep. Prog. Phys.* **2014**, *77*, 022601.
- (58) Malevanets, A.; Kapral, R. *J. Chem. Phys.* **1999**, *110*, 8605–8613.
- (59) Malevanets, A.; Kapral, R. *J. Chem. Phys.* **2000**, *112*, 7260–7269.
- (60) Kremer, K.; Grest, G. S. *J. Chem. Phys.* **1990**, *92*, 5057–5086.
- (61) Izaguirre, J. A.; Catarello, D. P.; Wozniak, J. M.; Skeel, R. D. *J. Chem. Phys.* **2001**, *114*, 2090–2098.
- (62) Ihle, T.; Kroll, D. *Phys. Rev. E* **2001**, *63*, 020201.
- (63) Ihle, T.; Kroll, D. M. *Phys. Rev. E* **2003**, *67*, 066705.
- (64) Lees, A.; Edwards, S. *J. Phys. C* **1972**, *5*, 1921.
- (65) Frenkel, D.; Smit, B. *Understanding molecular simulations: from algorithms to applications*; Academic Press, 1996.
- (66) Aust, C.; Kröger, M.; Hess, S. *Macromolecules* **1999**, *32*, 5660–5672.
- (67) Nikoubashman, A.; Likos, C. N. *Macromolecules* **2010**, *43*, 1610–1620.
- (68) Jaramillo-Cano, D.; Formanek, M.; Likos, C. N.; Camargo, M. *J. Phys. Chem. B* **2018**, *122*, 4149–4158.

- (69) Chen, W.; Chen, J.; An, L. *Soft Matter* **2013**, *9*, 4312–4318.
- (70) Winkler, R. G. *J. Chem. Phys.* **2010**, *133*, 164905.
- (71) Bossart, J.; Oettinger, H. C. *Macromolecules* **1995**, *28*, 5852–5860.
- (72) Doi, M.; Edwards, S. F. *The theory of polymer dynamics*; Oxford University Press: Oxford, U.K., 1986.
- (73) Link, A.; Springer, J. *Macromolecules* **1993**, *26*, 464–471.
- (74) Bird, R.; Curtiss, C.; Armstrong, R.; Hassager, O. *Dynamics of Polymer Liquids Vol. 2 Kinetic Theory*; Wiley, 1987.
- (75) Larson, R. G. *The Structure and Rheology of Complex Fluids*; Oxford University Press: Oxford, U.K., 1999.
- (76) Huang, C.; Chatterji, A.; Sutmann, G.; Gompper, G.; Winkler, R. *J. Comp. Phys.* **2010**, *229*, 168 – 177.
- (77) Huang, C.-C.; Sutmann, G.; Gompper, G.; Winkler, R. G. *EPL* **2011**, *93*, 54004.
- (78) Aust, C.; Hess, S.; Kröger, M. *Macromolecules* **2002**, *35*, 8621–8630.
- (79) Singh, S. P.; Fedosov, D. A.; Chatterji, A.; Winkler, R. G.; Gompper, G. *J. Phys.: Condens. Matter* **2012**, *24*, 464103.
- (80) Sablić, J.; Delgado-Buscalioni, R.; Praprotnik, M. *Soft Matter* **2017**, *13*, 6988–7000.
- (81) Eckart, C. *Phys. Rev.* **1935**, *47*, 552–558.
- (82) Huang, C.-C.; Winkler, R. G.; Sutmann, G.; Gompper, G. *Macromolecules* **2010**, *43*, 10107–10116.
- (83) Huang, C.-C.; Gompper, G.; Winkler, R. G. *J. Phys.: Condens. Matter* **2012**, *24*, 284131.

- (84) Fedosov, D. A.; Singh, S. P.; Chatterji, A.; Winkler, R. G.; Gompper, G. *Soft Matter* **2012**, *8*, 4109–4120.
- (85) Singh, S. P.; Chatterji, A.; Gompper, G.; Winkler, R. G. *Macromolecules* **2013**, *46*, 8026–8036.

SUPPORTING INFORMATION

Static and dynamic observables as a function of the Weissenberg number, for linear chains of $N = 200$ monomers

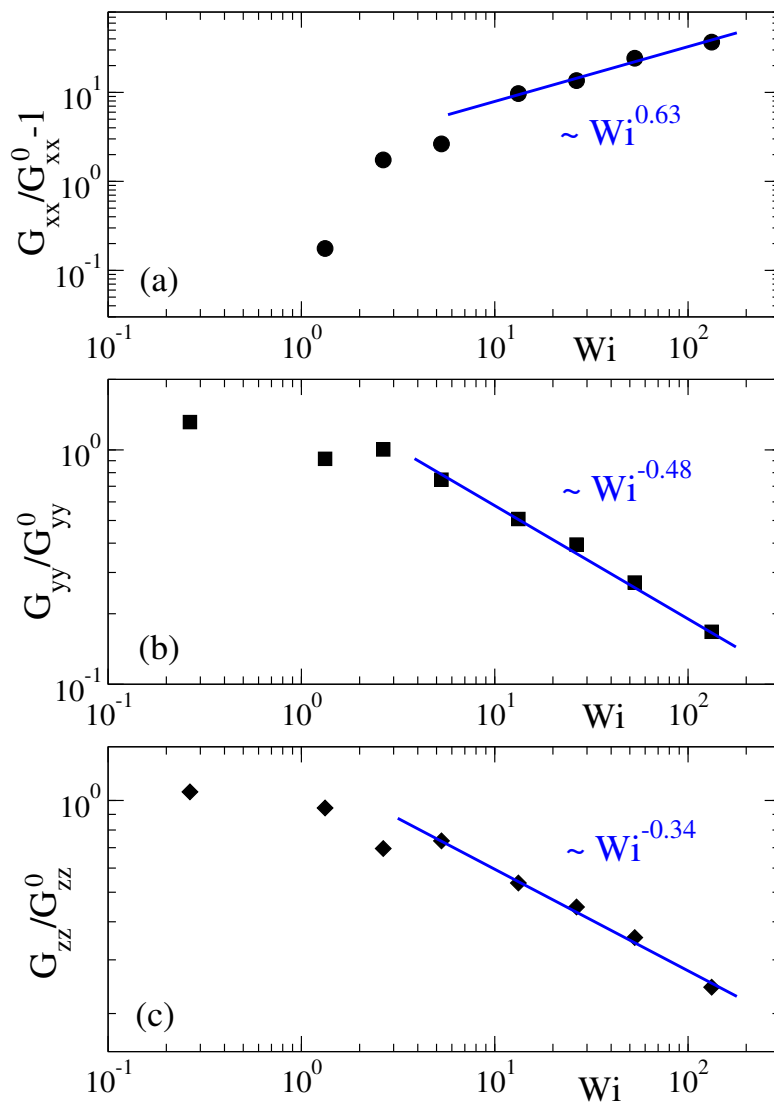


Figure S1. Normalized diagonal components of the gyration tensor.

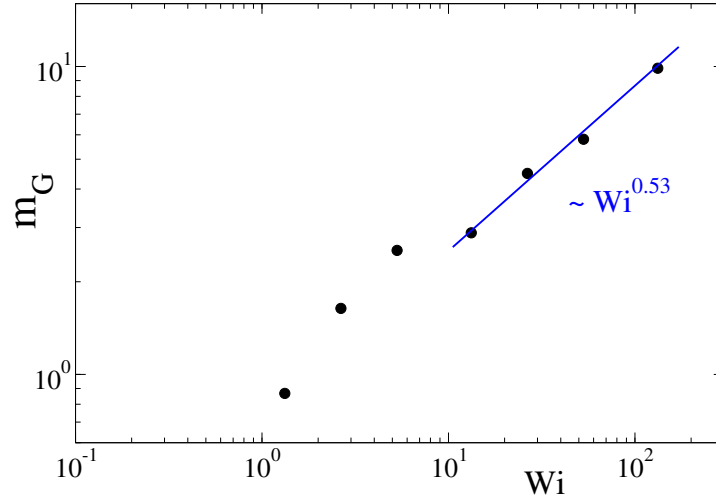


Figure S2. Orientational resistance.

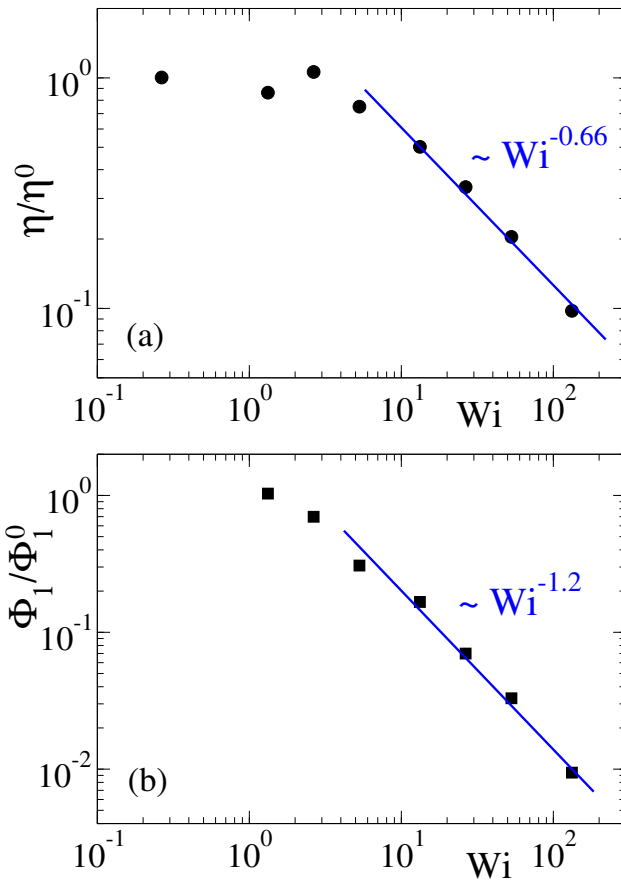


Figure S3. Normalized viscosity (a) and first normal stress coefficient (b).

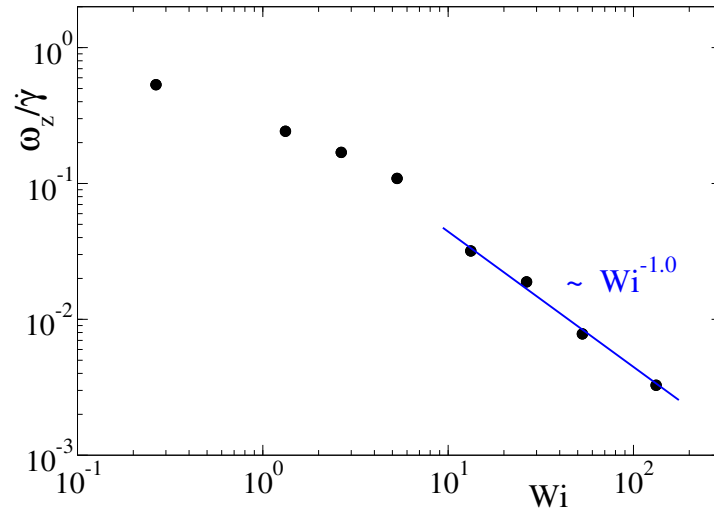


Figure S4. Rotational frequency.